THE JOURNAL OF PHYSICAL CHEMISTRY C

pubs.acs.org/JPCC Article

Using Electronic Sum-Frequency Generation to Analyze the Interfacial Structure of Singlet Fission-Capable Perylenediimide Thin Films

Daniel E. Cotton, Aaron P. Moon, and Sean T. Roberts*

Cite This: https://dx.doi.org/10.1021/acs.jpcc.0c01025 Read Online

ACCESS | Metrics & More | Article Recommendations | Supporting Information

ABSTRACT: Organic materials that undergo singlet exciton fission show promise as exciton multiplication materials for semiconductor solar cells by converting high-energy photons into pairs of spin-triplet excitons. However, singlet fission-based solar cells have experienced delayed implementation due to inefficient triplet transfer from organic light-absorbing layers to semiconductor energy acceptors, such as bulk silicon. As triplet transfer requires orbital overlap between the triplet-excited organic molecule and semiconductor energy acceptor, transfer will be dictated by the structure of the interface connecting these materials. Rational design and control of transfer requires detailed information about the structural and energetic environment of this buried interface, which is difficult to probe experimentally. To this end, electronic sum-frequency generation (ESFG), a noninvasive spectroscopy, can address this need by providing interface-selective information about both the molecular order and electronic structure of organic:semiconductor junctions. Here, we demonstrate ESFG's potential by comparing the buried interfacial structure of two singlet fission-capable perylenediimide derivatives deposited as thin films on glass. We find ESFG spectra signal a prominent narrowing of the bandgap of each perylenediimide derivative at the glass interface relative to their bulk, which we show is consistent with a subangstrom change in intermolecular packing at the buried interface. In addition, analysis of the polarization dependence of measured ESFG spectra shows that each derivative adopts different orientations of their perylene cores with respect to the substrate, which has important consequences for achieving exciton transfer across triplet-extracting semiconductor junctions.

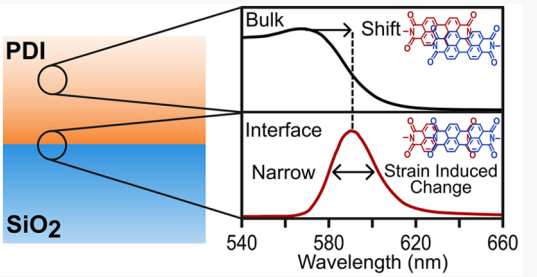

INTRODUCTION

Silicon photovoltaics dominate the solar energy market, accounting for >90% of solar installations.[1−3] While the cost of such installations has reduced significantly over the past decade,[1,2,4] silicon photovoltaic efficiency has remained largely static over the past 20 years.[3,5−7] For these cells, the largest loss mechanism is the thermalization of excited charge carriers to silicon's band edge.[2,5,6] Multijunction solar cells composed of complementary materials with different bandgaps can mitigate these losses, albeit while also increasing manufacturing expense and module complexity.[1,2] Instead, photon down-conversion via singlet fission (SF) presents a cost-effective alternative as SF can be used to create multiple electron−hole pairs from single photons.[2,8,9] SF is a process that occurs in select organic solids wherein a photogenerated spin-singlet exciton converts into two spin-triplet excitons, each with an energy roughly half that of the spin-singlet state.[10−15] This process can be quite fast,[16,17] and hence efficient, since SF conserves electron spin as the triplet pairs it creates are spin-correlated, with no net spin. Through careful consideration of its electronic structure, a SF-active material can be combined with a silicon solar cell to reduce energy lost by the device.[6,7,18,19]

Yet, while this idea was originally proposed in the late 1970s by Dexter,[18] only in 2019 has direct spin-triplet exciton transfer between organic molecules and silicon been confirmed.[19,20] As SF has been shown to be efficient in many materials,[16,21−27] this delayed development has been attributed to disfavored triplet exciton transfer from the organic sensitization layer to the underlying inorganic substrate.[3,6,19,28,29] The underlying reasons for poor transfer are not well-described and could arise from several material-dependent sources. For example, band bending or the presence of deleterious surface states at the interface between the organic sensitizer and silicon could lead to changes in the energetic landscape that prevent efficient exciton transfer.[7,19,29,30] Likewise, the morphology of the organic SF sensitizer itself at a junction could be a bottleneck, as triplet energy transfer necessitates wave function overlap between the

Received: February 6, 2020
Revised: May 1, 2020
Published: May 4, 2020

sensitizer and silicon. Because molecular wave functions are anisotropic, transport properties and energetics at the interface are likely sensitive to molecular orientation.[7,24,31−37] Moreover, when deposited as a thin film, organic dyes can experience strong energetic coupling between individual molecules, causing the electronic states of the film to greatly differ as a function of how these molecules arrange themselves.[31,35,36] Thus, any changes in the morphology of the molecular system at a silicon junction could induce a shift in the organic solid's triplet energy relative to the film's bulk. If such a shift places the triplet state lower in energy than silicon's bandgap, this will create an energetic barrier for triplet transfer.[7,24,31,37−39]

To identify the key bottlenecks in organic-to-silicon energy transfer, there is a critical need to determine how the electronic structure of the organic SF sensitizer is altered when placed into contact with silicon. Addressing this problem is challenging as it requires measurement of a buried interface. Conventional probes such as electronic absorption and photoelectron spectroscopy,[40] scanning probe measurements,[41−43] and X-ray diffraction and related scattering techniques are either more sensitive to the bulk of an organic film grown on silicon or limited to exposed interfaces rather than buried ones. Electronic sum-frequency generation is a fantastic tool that can fill the gap left by these experimental tools.

Electronic sum-frequency generation (ESFG) is a measurement technique that selectively interrogates the electronic density of states and structural organization of molecular junctions and has been used to study liquid surfaces,[44−47] semiconductor surfaces,[48−50] and buried organic:inorganic junctions.[51−55] In an ESFG measurement, two pulses of light simultaneously impinge on a sample. One of these pules is a spectrally broad white light (WL) continuum that overlaps with different electronic resonances within the sample. The other is a spectrally narrow upconversion pulse whose frequency is set far from electronic resonance with the sample. The sample acts to mix these two pulses together, producing light at their sum frequency. As resonance between the WL pulse and electronic states within the sample enhances this mixing process, the ESFG spectrum reports on the sample's electronic density of states. Importantly, because of symmetry restrictions, the mixing process that produces ESFG selectively occurs at regions of a sample that lack inversion symmetry,[56] which is naturally satisfied at organic:inorganic junctions. Because of this selection rule, ESFG provides spectral information analogous to an interfacial absorption spectrum. Moreover, the dependence of the polarization of the emitted ESFG field on that of the excitation fields reports the hyperpolarizability of molecules at buried interfaces, which can be decomposed into a product of the molecules' transition dipole moment and polarizability.[45,52,57,58] If the mapping of these parameters onto the molecular frame is known, it is possible to determine from ESFG spectra the spatial orientation of molecules at buried interfaces.

Here, we report ESFG spectra of perylenediimide (PDI) thin films. We choose to examine this class of materials as PDIs have several qualities that make them attractive for use as SF sensitization layers for silicon solar cells. First, our group and others have shown PDIs readily undergo SF in the solid state.[23,59] Importantly, the PDI triplet energy (1.1−1.2 eV)[31,59] is near ideal for sensitization of silicon. PDIs are also highly resistant to photooxidation,[60] have large molar extinction coefficients (50000−100000 M^{-1} cm^{-1})[23,61−65] that enable thin PDI coatings to absorb a significant fraction of incident visible light, and can be easily functionalized to form various derivatives with distinct solid-state structures and unique electronic state densities. By use of simple tight-binding models,[36,40] the optical absorption spectrum of a PDI film becomes a signifier of its underlying molecular packing (*vide infra*). Such structural control over molecular packing could likewise be used to optimize SF and triplet transfer to silicon, as the same intermolecular couplings that govern optical absorption control relaxation kinetics.[31,40,66]

In this report, we examine two PDI derivatives deposited as thin films on fused silica substrates to determine how their side chains direct packing at a buried interface. This work serves as a prelude for studies of films on silicon. Understanding the structure of PDI:SiO_2 interfaces is also key as silicon oxide is a common surface impurity formed when preparing functionalized silicon surfaces, and the packing structures adopted by PDIs on nonpolar SiO_2 surfaces are expected to be not unlike those they can adopt on mixed metal oxide/metal nitride interfaces employed to achieve spin-triplet exciton transfer from SF materials to silicon.[19] As we show below, strain-induced changes in packing can strongly modify the electronic structure of PDI derivatives at a buried surface. Thus, altering PDI side groups provides us with an effective handle to manipulate the electronic structure of PDI films at these key junctions and optimize them for spin-triplet exciton transfer.

The paper is outlined as follows. The Experimental Methods section details techniques used to prepare and characterize PDI thin films, which includes a description of our ESFG spectrometer with an emphasis placed on improvements made to it following our last ESFG report.[51] The Results section begins by showing the bulk crystal structure of our PDI thin films along with the output of our tight-binding model, which we use to compute the films' bulk electronic structure. We then discuss our observed ESFG spectra and the application of a thin-film interference model[52,67] to this data to extract the portion of the signal that originates from the buried PDI:SiO_2 interface. We finally analyze a pronounced narrowing of the PDI bandgap at the SiO_2 interface indicated by our ESFG spectra, which we conclude is consistent with a subangstrom shift in PDI crystal packing. Taken togther with our polarization measurements, this indicates a subtle change in molecular packing at the PDI:SiO_2 interface compared to the bulk PDI structure, which arises from strain induced by the dissimilar environment interfacial molecules experience compared to the bulk.

EXPERIMENTAL METHODS

Thin Film Preparation and Characterization. PDI Films were grown following our previously published procedure.[24] *N,N′*-Dimethyl-3,4,9,10-perylenedicoarboximide (C1-PDI, 98%, Scheme 1, red) and *N,N′*-dioctyl-3,4,9,10-perylenedicarboximide (C8-PDI, 98%, Scheme 1, blue) were purchased from Sigma-Aldrich and used as received. Polycrystalline thin films were grown on UV-fused silica substrates by using a thermal evaporator (AMOD PVD system, Ångstrom Engineering) at a deposition rate of ∼1 Å/s under ambient temperature and 10^{-6}−10^{-7} Torr. We also concurrently grew films on native-oxide-capped (∼2 nm thick) p-type silicon (100) wafers. PDI film thickness was determined by using variable angle spectroscopic ellipsometry (M-2000 ellipsometer, J.A. Woollam) on films grown on silicon (100) over a wavelength range of 900−1600 nm, which was

https://dx.doi.org/10.1021/acs.jpcc.0c01025
J. Phys. Chem. C XXXX, XXX, XXX−XXX

Scheme 1. Molecules Investigated in This Report

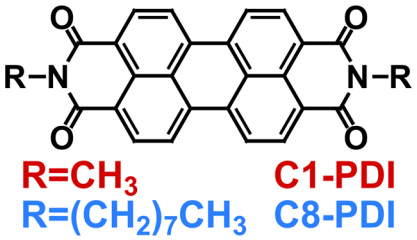

subsequently fit to a multilayer Cauchy model. Grazing-incidence wide-angle X-ray scattering (GIWAXS) was performed by using a SAXSLAB Ganesha equipped with a Dectris 300K detector and a Cu Kα source (λ = 1.5418 Å). During scattering measurements, films were angled between the substrate and film critical angle (ω = ~0.1° to ~0.3°). Data were reduced by using the manufacturer supplied analysis program SAXSGUI. Reflection-corrected absorption spectra were taken on a Shimadzu UV-2600 absorption spectrometer with an integrating sphere attachment.

ESFG Measurements. The experimental layout employed for ESFG is shown in Figure 1A. A femtosecond Ti:sapphire regenerative amplifier (Coherent Legend Elite Duo, 3 kHz, 4.5 mJ) was used to generate a 90 fs pulse centered at 804 nm with a bandwidth of 160 cm^{-1} (fwhm). A small portion of the amplifier output (0.1 mJ) was focused into a 1 cm path length water flow cell (Starna Cells, 46-Q-10) to generate a white-light supercontinuum (WL) that was subsequently collimated with a 90° off-axis parabolic mirror (MPD129-G01, Thorlabs). The water temperature was maintained at 13.2 °C by using a chiller (Thermotek T255P) for optimal WL generation. The WL spectrally extends from ~350 nm to the fundamental 804 nm. After spectral filtering, the remaining portion of the WL (450–750 nm) spectrally overlaps with the visible absorption features of C1-PDI and C8-PDI films (Supporting Information Figure S5).

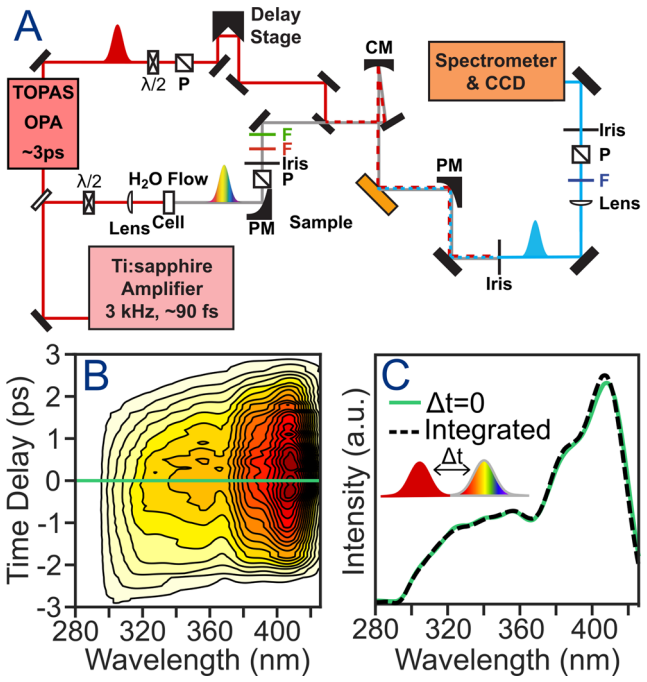

Figure 1. (A) ESFG spectrometer layout. F: filter; P: polarizer; CM: curved mirror; PM: parabolic mirror. (B) ESFG spectra of *z*-cut quartz measured as a function of the time separation between the upconversion and WL pulses. (C) Comparison spectrum taken at a single time point (Δt = 0, green) and the temporally integrated sum (black dashed line) across the cross-correlation in panel B. The overlap of these spectra shows there is no need to sweep the time separation between the WL and upconversion fields to capture an ESFG spectrum that uses the full WL spectral bandwidth.

We generated the upconversion pulse using a second portion (~1.5 mJ) of the amplifier output to first produce a spectrally narrow 400 nm pulse using a second harmonic bandwidth compressor (SHBC-400, Light Conversion). This pulse in turn pumped an optical parametric amplifier (TOPAS-400, Light Conversion), producing ~3 ps shortwave infrared pulses whose center wavelength could be tuned for a given experiment. This ability to vary the upconversion pulse's frequency is key to accounting for double-resonance effects caused by electronic resonance of the ESFG field with high-energy electronic states within a sample (*vide infra*).[44,45] Importantly, the temporal length of the upconversion pulse is sufficiently long to allow it to temporally overlap with the full spectral bandwidth of the WL field despite substantial temporal chirp in the latter (Figure 1B,C). This represents a significant improvement over our prior ESFG setup, which used an ~100 fs 800 nm pulse as the upconversion field that necessitated scanning the path length traveled by this pulse relative to the WL field to fully record a sample's ESFG spectrum.[51,52]

The upconversion and WL fields were focused onto the sample using a 15 cm focal length concave mirror in a noncollinear geometry. Spectra were measured in a reflection geometry by using an angle of incidence of 45° with respect to the sample surface normal for both the WL and upconversion fields. The wavevectors of both incident fields were tilted slightly out of the plane of incidence (±2.5°–5°), which allowed spatial separation of the ESFG signal from the driving fields. The ESFG signal was collected and collimated with a 90° off axis parabolic mirror (50331AL, Newport) and passed through irises to remove scattered WL. A 50 cm lens focused the ESFG field onto the entrance slit of a spectrometer (Acton Spectra Pro SP-2500) where a 300 groove/mm grating blazed at 300 nm spectrally dispersed the signal onto a 512 × 2048 pixel liquid nitrogen cooled CCD (PyLoN, Princeton instruments).

To avoid sample damage, the pulse energies used for C1-PDI measurements were 2.1 μJ for the WL beam and 12.5 μJ for the upconversion field. For C8-PDI measurements, these values were lowered to 0.7 and 8 μJ, respectively. PDI ESFG spectra recorded by using pulse energies up to these values were found to be reproducible day to day. Unless otherwise noted, the wavelength of the upconversion field was set to 885 nm. Spectral acquisition times for each film were held fixed for polarization measurements performed on each derivative but varied between derivatives, with 2 min/spectrum for C1-PDI and 5 min/spectrum for C8-PDI. All ESFG spectra were normalized by a reference spectrum of a *z*-cut quartz piece placed at the sample position to account for spectral variation of the WL field and the spectral sensitivity of our ESFG spectrometer.

In all ESFG measurements, the polarizations of the WL, upconversion pulse, and emitted ESFG were selected by using half-wave plates and polarizers shown in Figure 1A. The polarization combination listed for a given ESFG spectrum

https://dx.doi.org/10.1021/acs.jpcc.0c01025
J. Phys. Chem. C XXXX, XXX, XXX–XXX

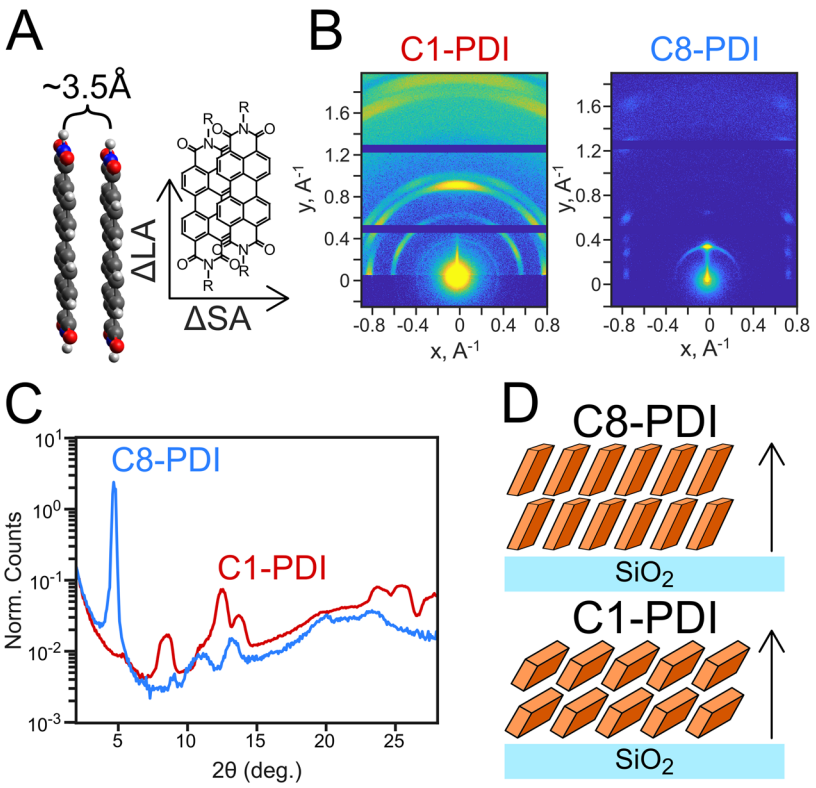

Figure 2. (A) Diagram showing the slip-stacked packing structure common to PDI derivatives. Nearest-neighbor PDI molecules tend to be separated by ~3.5 Å, with short axis (SA) and long axis (LA) displacements set by their imide side chains (R). (B) GIWAXS diffractograms of ~200 nm thick C1-PDI (left) and C8-PDI (right) films grown on SiO_2. (C) Corresponding azimuthally integrated diffractogram for both derivatives, converted to 2θ for ease of comparison to existing literature. The diffuse scattering ring at ~1 $Å^{-1}$ (22° in both images is due to the SiO_2 substrate. (D) Dominant orientation of the perylene cores of C8-PDI and C1-PDI on SiO_2 as determined by GIWAXS.

describes in order the polarization of the ESFG, upconversion, and WL fields. Thus, in our notation a "SSP" measurement corresponds to detection of the s-polarized component of the ESFG field generated by an s-polarized upconversion field interacting with p-polarized WL.

RESULTS AND DISCUSSION

Bulk Properties of PDI Solids. Before characterizing the interfacial structure of C1-PDI and C8-PDI thin films, we first examine the structure of their bulk using grazing-incidence wide-angle X-ray scattering (GIWAXS) and optical absorption spectroscopy. Both C1-PDI and C8-PDI are known to adopt crystal structures with PDI molecules arranged in 1D columns with differing degrees of slip displacement between neighboring molecules but with similar separation between neighboring perylene cores (d = ~3.5 Å; see Figure 2A for a schematic representation).[68,69] When deposited as thin films on SiO_2, we have previously shown these materials form polycrystalline solids wherein the structure of the crystallites retains much of the order seen in single crystals of each material.[24]

GIWAXS measurements of the C1-PDI and C8-PDI films grown for this study highlight this polycrystalline structure (Figure 2B). Azimuthally integrated diffractograms for ~200 nm thick C1-PDI and C8-PDI films are shown in Figure 2C and exhibit peaks suggesting oriented growth of PDI crystallites, consistent with prior reports for C1-PDI[69−71] and C8-PDI[68,72,73] films grown by using deposition conditions similar to those we employ. Compared to the computed powder diffraction pattern, the (002) plane for C1-PDI is enhanced, indicating C1-PDI films preferentially grow with the long perylene axis parallel to, and the short axis tilted toward, the substrate surface (Figure 2D, bottom).[74] C8-PDI films meanwhile adopt a more lamellar structure, with enhancement of the (001) plane, as previously noted by others[72] (Figure 2D, top). These films display a series of peaks at $q_{\|} \sim \pm 0.8$ $Å^{-1}$ (Figure 2B, right) that we attribute to various orders of the {101} family plane along the direction perpendicular to the substrate. The well-resolved appearance of these peaks implies the presence of oriented crystallites within C8-PDI films.[72] In contrast, the broad peaks and diffusive rings featured in the C1-PDI film diffractogram indicate orientational disorder among the crystallites within the film.

Figure 3 plots optical absorption spectra of ~50 nm thick C1-PDI and C8-PDI films. The absorption envelope for each derivative displays a four-peaked structure that differs in its overall bandwidth and peak intensity pattern. The absorption profile of C1-PDI (Figure 3A) shows a peak at 568 nm with a weak companion peak at 540 nm along with a strong pair of peaks at 480 and 468 nm. In comparison, C8-PDI (Figure 3B) exhibits a comparatively weak peak at 565 nm, a stronger shoulder at ~540 nm, and a pair of peaks at 480 and 468 nm that are similar to those in spectra of C1-PDI. Notably, both films possess low-energy tails of varying length. This tail has previously been postulated to arise from minority states created during film deposition,[74,75] a hypothesis we believe to be consistent with our ESFG results (*vide infra*).

The similar peak structure and placement contrast with the subtle difference in overall bandwidth between the two derivatives as well as the ordering of peak intensity. Although these derivatives both form slipped 1D columnar stacks in their

https://dx.doi.org/10.1021/acs.jpcc.0c01025
J. Phys. Chem. C XXXX, XXX, XXX−XXX

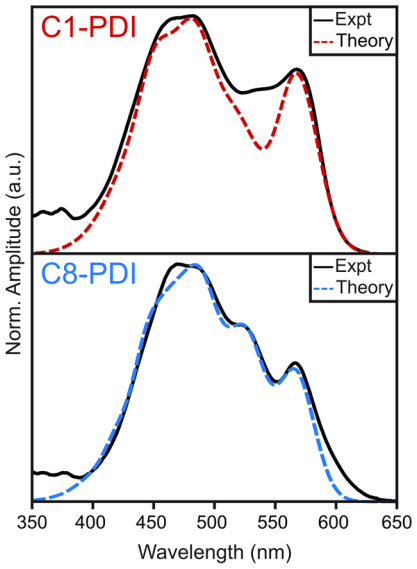

Figure 3. Absorption spectra (solid line) of an ∼50 nm thick C1-PDI (A) and C8-PDI (B) films grown on SiO_2 along with fits (dashed line) produced using a tight-binding Hamiltonian model.

crystal structure,[68,70] their side groups induce differing degrees of slip within these columns, altering the electronic coupling between molecules in a stack. These subtle packing shifts modulate the coupling between neighboring molecules that dictate their resulting optical properties.[66,76,77]

Knowing the slip-stack geometry our PDI films adopt allows us to analyze their absorption spectra using a tight-binding Hamiltonian (see the Supporting Information for full details). Within this model, excitonic couplings correspond to Coulombic dipole−dipole interactions, while charge-transfer coupling is facilitated by electron/hole transfer integrals. As the charge-transfer interactions are dependent on wave function overlap, they depend on frontier orbital symmetry. Thus, the charge-transfer couplings follow the nodal structure and phasing of the molecular orbitals, causing displacements smaller than the size of the molecule to have drastic effects on the couplings.[35,36] This variation in coupling has been used to describe the pronounced crystallochromy seen between different PDI derivatives.[66,76] In addition to the charge-transfer coupling, the relative energetic spacing between the charge-transfer and Frenkel exciton states greatly affects each derivative's solid-state absorption spectrum.[40,76,78]

Within our Hamiltonian, we have two unknown parameters that cannot be experimentally determined: the energy difference between a nearest-neighbor charge-transfer state and the ground state, ϵ_{CT}, and the energetic relaxation of the monomer as it transfers from solution to a more polarizable crystalline environment, $\Delta_{S\rightarrow C}$. We found the C1-PDI and C8-PDI spectra can be well reproduced using values for these parameters similar to those reported elsewhere (Figure 3, dashed line; see the Supporting Information for parameter values).[40] In particular, the absorption bandwidth and relative intensity of the major peaks of both derivatives are recovered. Note that this model does not account for high-energy peaks that arise from the well-known $S_0 \rightarrow S_2$ transition, which contributes to experimental spectra in Figure 3 at wavelengths <400 nm.[77] As we show below, this band influences ESFG spectra of C1-PDI and C8-PDI via double-resonance signal enhancement.

ESFG Spectra of PDI Film Interfaces. Using ESFG, we can determine the extent to which differences in the electronic and molecular structure of C1-PDI and C8-PDI highlighted above extend to the interfaces they form with SiO_2. Figure 4

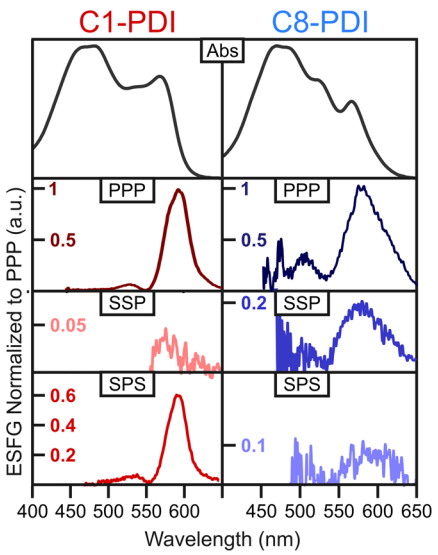

Figure 4. Comparison of ESFG and optical absorption spectra (Abs) of a 51 nm thick C1-PDI film (left column) and 72 nm thick C8-PDI film (right column). ESFG spectra of each PDI derivative are normalized in intensity to their corresponding PPP spectrum.

shows ESFG spectra of a 51 nm thick C1-PDI film and a 72 nm thick C8-PDI film collected by using PPP, SPS, and SSP polarization conditions. PSS spectra were also measured but were found to be negligible in intensity. All ESFG spectra are normalized to the strongest peak in the PPP spectrum of each derivative to highlight differences in the intensity of spectra measured for each polarization combination. Figure 4 also compares ESFG spectra to the optical absorption spectrum of each film (top). To facilitate this comparison, we have subtracted the energy of the 885 nm upconversion pulse from the wavelength axis of the plotted ESFG spectra.

The ESFG data suggest drastic differences in the interfacial density of states of each film relative to that of their bulk. In contrast to the broad absorption bandwidth shown by both PDI derivatives, ESFG spectra for each derivative are decidedly narrower. Most notable is the PPP spectrum of C1-PDI, which displays a prominent peak that is red-shifted relative to the onset of its bulk absorption spectrum. Only a small sideband, peaked at ∼525 nm, falls within the bandwidth of the film's bulk absorption spectrum. ESFG spectra of C8-PDI are more complicated, displaying a broader set of peaks. Like C1-PDI however, the onset of the C8-PDI PPP spectrum also falls below that displayed by its bulk absorption spectrum. These observations suggest changes in the electronic structure of each film when moving from their bulk to the SiO_2 interface.

The relative intensities of ESFG spectra recorded for different polarization conditions are also found to vary between the two PDI derivatives. While the PPP spectrum of each derivative yields the strongest ESFG signal, the relative amplitudes of the SSP and SPS spectra differ for the two derivatives. For C1-PDI, the SPS spectrum is found to be nearly as intense as that of the PPP spectrum while the SSP signal is negligibly small. In contrast, the SSP signal for C8-PDI is 2× stronger that than of the film's SPS signal but 5× weaker

https://dx.doi.org/10.1021/acs.jpcc.0c01025
J. Phys. Chem. C XXXX, XXX, XXX−XXX

than that of the PPP signal. These differences in signal strength for different polarization conditions hint at differences in molecular ordering of each film at the SiO_2 interface.

Before we can map the ESFG spectra to their underlying molecular origin, we must first deconvolute local field effects from the data. As PDI thin films necessarily contain two regions that lack inversion symmetry, the exposed air:PDI surface and buried PDI:SiO_2 interface, ESFG spectra in Figure 4 can contain contributions from both regions. At a detector, these signals will interfere, leading to either constructive or destructive modification of ESFG spectra. Data reported by us[52] and others[79−81] have shown this can modify ESFG spectra of thin organic films. Figure 5 highlights this complication by

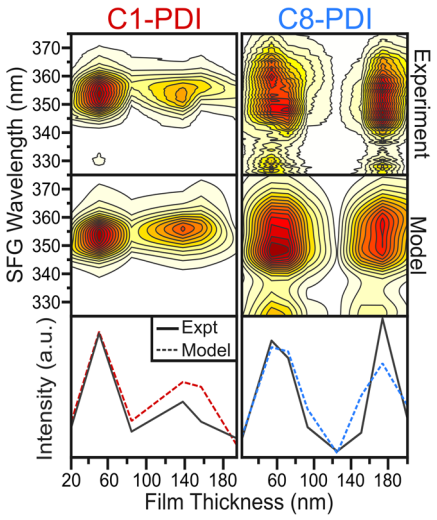

Figure 5. Experimental PPP ESFG spectra of C1-PDI and C8-PDI films as a function of film thickness (top) compared to results from an interference model (middle). (Bottom) Spectrally integrated ESFG intensity as a function of film thickness (solid line) compared against that predicted by the interference model (dashed line).

showing the measured PPP-polarized ESFG spectra of C1-PDI and C8-PDI films measured for films with thicknesses ranging from ∼20 to ∼200 nm. Looking at the series of ESFG spectra for C1-PDI (Figure 5, top left), we see the first strong ESFG signal for a film thickness of ∼50 nm, a trough at ∼110 nm, and a recurrence at ∼140 nm for the main ESFG emission wavelength of 355 nm. This beating pattern stems from signals produced by the air:PDI and PDI:SiO_2 interfaces moving in and out of phase. We see a similar pattern for C8-PDI with maxima at film thicknesses of ∼60 and ∼175 nm (Figure 5, top right).

Fortunately, we can recover the intrinsic response from the buried PDI:SiO_2 interface of each derivative by using a thin film interference model based on transfer matrices to calculate the electric field at each film interface, apply a complex susceptibility response, and fit our experimental ESFG data.[52,80−83] The thin film modeling fit to the C1-PDI spectra agrees well with the modulation in ESFG bandwidth at thicker films (Figure 5, middle left) and produces the same trends in total intensity of the ESFG response when integrating across the ESFG wavelength axis (Figure 5, bottom left). While discrepancies between experiment and the fit are apparent for film thicknesses >100 nm, the fit reproduces well the overall trend of the data. We show a similar fit to the C8-PDI ESFG data in the right column of Figure 5. The model broadly agrees with the lower-energy, high-intensity portion of the PPP spectrum, with peaks that occur at identical thickness regions to that of the experiment. However, the reoccurrence of the lower-energy peak is somewhat weaker than that seen experimentally (Figure 5, bottom right).

One potential origin for our model's reduced performance in matching the spectral amplitude of higher thickness PDI films could arise from electric quadrupole contributions to each material's nonlinear susceptibility.[80,84,85] Such contributions are bulk active and, if present, would affect thicker films more than thinner films.[86] However, these terms should possess a PSS contribution.[85,87,88] As we see no appreciable PSS polarized ESFG signal, nondipolar terms seem unlikely to meaningfully contribute to our spectra. More likely, the difference in strength at the reoccurrence is due to a change in the ESFG response from the exposed air:PDI interface. As the surface roughness of PDI films is known to increase as film deposition occurs,[74,89,90] the ESFG signal from the air:PDI interface may decrease with increasing film thickness due to a net loss of crystallite orientation induced by stacking fault formation. We previously hypothesized formation of such stacking faults underlies differences in the second-order nonlinear susceptibility associated with the buried and air-exposed interfaces of copper(II) phthalocyanine thin films.[52] Indeed, such an effect was noted by Massari and co-workers when analyzing vibrational sum-frequency generation spectra for C8-PDI.[79]

Although Figure 5 only highlights experimental data and fits corresponding to PPP polarization conditions, we have also applied our interference model to data recorded using other polarization conditions. Fits to SPS and SSP data are shown in the Supporting Information along with a description of constraints applied when fitting these data sets. The spectral responses shown below in Figures 6, 9, and 10 are the result of these fits.

Polarization Dependence of ESFG Spectra. The polarization dependence of ESFG spectra is dictated by the

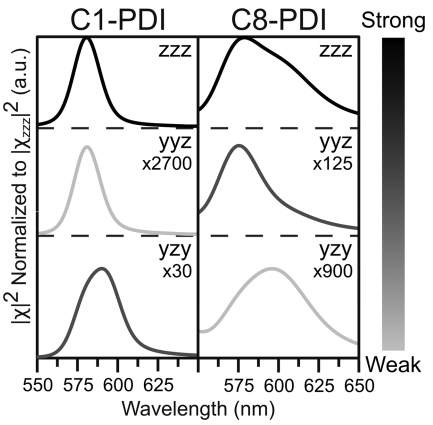

Figure 6. Polarization dependence of the extracted susceptibilities for the PDI:SiO_2 interface. Left: the nonzero susceptibility elements extracted from our interference model for C1-PDI films. Right: the same elements for C8-PDI films. The trio of letters denotes the susceptibility tensor element being plotted, and the lines are color coded to denote the relative amplitudes of different elements. Plotted values for $|\chi_{yzy}|^2$ and $|\chi_{yyz}|^2$ for each PDI are normalized relative to the maximum value extracted for $|\chi_{zzz}|^2$. Values listed in the upper right corner indicate the multiplicative factors that need to be applied to $|\chi_{yzy}|^2$ and $|\chi_{yyz}|^2$ to have their intensity match that of $|\chi_{zzz}|^2$.

https://dx.doi.org/10.1021/acs.jpcc.0c01025
J. Phys. Chem. C XXXX, XXX, XXX−XXX

degree of anisotropy within a sample's second-order nonlinear susceptibility tensor, $\chi^{(2)}$. By comparing the relative strengths of each element of the $\chi^{(2)}$ tensor and mapping these susceptibility elements to the molecular properties they arise from, we can extract information about the orientation of PDI molecules at a buried surface.[58,82,91,92] Using the excited-state perturbation method[93] and assuming enhancement of ESFG spectra arises purely from resonance between a sample's electronic states and frequency components of the WL field, we can decompose the tensor elements of $\chi^{(2)}$ as $\chi_{ijk} = \alpha_{ij}\mu_k$, where μ_k is the sample's transition dipole moment associated with the resonant interaction with the WL field and α_{ij} is the sample's polarizability associated with the frequencies of the nonresonant pulse and emitted ESFG field.[94,95] Using this formulation, the χ_{yzy} element of the $\chi^{(2)}$ tensor is $\chi_{yzy} = \alpha_{yz}\mu_y$, the product of the projection of the film's transition dipole parallel to the substrate with a portion of its out-of-plane polarizability. Likewise, $\chi_{yyz} = \alpha_{yy}\mu_z$ reports the product of the system's in-plane polarizability and out-of-plane dipole. The ratio of these two polarizations has been used to measure the tilt of transition dipole moments associated with molecular vibrational modes from surface normal under the assumption that the system adopts in-plane azimuthal symmetry.[82,92] While our GIWAXS data show oriented growth of PDI crystallites along the surface normal, the diffuse ring attached to each C1-PDI diffraction peak and the (001) peak for C8-PDI indicates these crystallites are randomly oriented within the plane parallel to the sample surface. This allows us to apply azimuthal symmetry to our sample analysis. Under this assumption, the in-plane coordinates, x and y, are interchangeable, while the coordinate normal to the substrate, z, is unique. Full details on how these "molecular frame" coordinates map onto the polarization of our fields can be found in the Supporting Information and ref 94.

The polarization dependence of $\chi^{(2)}$ reflects the macroscopic electronic structure of our PDI films, which in turn is set by the degree of electronic coupling between individual molecules within each film.[94] As we lack a quantitative calculation of how intermolecular coupling alters the polarizability tensor associated with PDI electronic states, we refrain from attempting to extract from polarization-dependent ESFG spectra a full quantitative description of the orientation adopted by C1-PDI and C8-PDI films at the SiO_2 interface. However, under the assumption of weak Davydov splitting between molecules, the orientation of the principal transition moments and the polarizability response of the coupled system are not expected to strongly deviate from that of uncoupled PDIs. While this is perhaps a crude approximation, for the purposes of the present discussion this allows us to use the properties of PDI monomers as a basis for interpreting the polarization dependence of our ESFG spectra.

The transition moments of monomeric C1-PDI and C8-PDI are nearly identical. Each molecule possesses a primary transition dipole moment associated with their lowest-energy dipole-allowed transition ($S_0 \rightarrow S_1$) that is nearly exclusively oriented along the long axis of their perylene core.[76] The ground-state static (zero frequency) polarizability of each molecule is also similar, being largest along the perylene long axis, followed next by the perylene short axis, and then the out-of-plane direction (normal to the aromatic plane). We use this static polarizability to qualitatively approximate the orientation of each PDI's frequency-dependent polarizability contributions to their $\chi^{(2)}$ tensor.[96,97]

The left portion of Figure 6 provides the extracted polarization dependence of the C1-PDI films at the buried PDI:SiO_2 interface, which reveals $|\chi_{yzy}|^2$ dominates $|\chi_{yyz}|^2$ in intensity. As the transition dipole of C1-PDI monomers lie along the long axis of their perylene core, this suggests C1-PDI molecules orient in either a face-on or an edge-on manner with their long axis parallel to the SiO_2 substrate. The preference for one of these geometries over the other can be determined by noting the polarizability of C1-PDI monomers is larger along the perylene short axis than in the direction normal to the plane of the perylene core, which favors molecules aligning in an edge-on manner (Figure 2D). In contrast, a comparison of the susceptibility elements for C8-PDI (Figure 6, right panels) show an opposite ordering of intensities, with $|\chi_{yyz}|^2$ being ~10× larger than $|\chi_{yzy}|^2$. This intensity ordering suggests C8-PDI molecules adopt an orientation at the SiO_2 interface where the long axis of their perylene core orients at an angle to the surface normal, so that the in-plane and out-of-plane components of the C8-PDI transition dipole each contribute to the ESFG response. This orientation analysis agrees well with the data gathered via X-ray diffraction, where the perylene core for C8-PDI is oriented ~60° from surface normal.[72,73,90] While we have admittedly made some crude assumptions in interpreting our ESFG spectra, analysis of the spectra provides a picture of the interfacial structure of both C1-PDI and C8-PDI films consistent with the texturing of these films along their surface normal inferred from GIWAXS data in Figure 2. Thus, structures adopted by both C8-PDI and C1-PDI molecules at the SiO_2 interface appear to form templates for the oriented growth of each film.

For both derivatives, χ_{zzz} is the strongest susceptibility by far. To a certain extent, this is expected. Simpson and co-workers found that for vibrational SFG, χ_{zzz} can be inherently 2× (or more) larger than other susceptibility elements after orientational averaging of the molecular hyperpolarizability and the symmetry of the transition are taken into account.[94] However, we note care should be taken in interpreting the large value of χ_{zzz} reported by our fitting routine. Information on χ_{zzz} comes solely from the PPP spectrum of each derivative, which is dependent on χ_{zzz} as well as χ_{yyz}, χ_{yzy}, and χ_{zyy}. Analysis of the local field strengths at each interface shows the Fresnel coefficients associated with the p-polarized fields that allow χ_{zzz} to contribute to the PPP ESFG spectrum are an order of magnitude weaker than other contributions to the PPP response from other tensor elements. As our model made no assumptions of the relative strength of the different susceptibilities, it found χ_{zzz} needed to be overwhelmingly strong to have any impact on the spectrum. Even with this large value, the χ_{zzz} contribution to the PPP spectrum of each derivative was very small. Indeed, going so far as to set χ_{zzz} to zero left the resulting spectra largely unchanged. Given this fact, we conclude that our spectra are not sensitive to χ_{zzz}. While we report the values of χ_{zzz} extracted from our interference model as they do improve the fit to our data, we caution that we need a more precise understanding of the local symmetry that creates our ESFG response, along with more intricate theory, to bound χ_{zzz}.

Double-Resonance Contributions to ESFG Spectra. Having established the ESFG polarization dependence agrees with structural data if we assume the ESFG is resonantly enhanced by a dipole-allowed, low-energy transition, we can now analyze the interfacial electronic structure. When we compare the C1-PDI tensor elements to the bulk absorption

https://dx.doi.org/10.1021/acs.jpcc.0c01025
J. Phys. Chem. C XXXX, XXX, XXX−XXX

spectrum of a C1-PDI film, we see a strong reduction in spectral bandwidth, with a greatly reduced number and placement of peaks in the ESFG data compared to the absorption spectra (Figure 4). In addition, there is a general red-shift, with the strongest ESFG peak appearing at λ_{WL} = 585 nm vs the first absorption peak at 568 nm for C1-PDI, an ∼50 meV shift. This notable red-shift places the maximum of the C1-PDI ESFG spectrum near the low-energy onset of the film's bulk absorption spectrum, suggesting the electronic states viewed via ESFG may correspond to "low-energy trap states" previously postulated by Jones and Ferguson.[74] C8-PDI films show similar differences between ESFG and absorption spectra.

Given the polarization dependence of the ESFG signal of each derivative tracks with the orientation of the transition dipole moment of their lowest excited singlet state, it is natural to assume this state is solely responsible for the resonance enhancement of the ESFG signal. On the other hand, ESFG spectra of each film are reduced in spectral bandwidth compared to their absorption spectra. As our WL pulse has sufficient bandwidth to cover the entire band-edge region of our films (Figure S5), it seems strange their ESFG spectra should be dominated by only a single resonance. However, we note that the frequency of the emitted ESFG field falls close to low-amplitude peaks within each film's absorption spectrum associated with their $S_0 \rightarrow S_2$ transition. Thus, there is a chance that the ESFG signal is dictated by either a two-photon or a double-resonance condition (Figure 7), each of which would not follow the same behavior as a one-photon resonant ESFG response.[94]

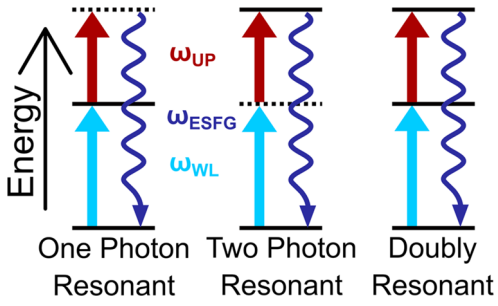

Figure 7. Different resonance conditions that can give rise to ESFG spectra. Dotted lines denote virtual states, and solid lines denote electronic states of the sample. ω_{WL}, ω_{UP}, and ω_{ESFG} denote frequency components of the white light, upconversion, and emitted ESFG fields.

To discern the origin of our response, we varied the frequency of our upconversion pulse, as the three resonance conditions will differ in how they adapt to changes in the photon energy of the upconversion field. Under the one-photon resonance condition (Figure 7, left), the upconversion pulse is used to nonresonantly upshift a resonance driven in the sample by the WL field. As the upconversion pulse is nonresonant, as its frequency is scanned the frequency of the ESFG field should linearly shift with it. In contrast, a two-photon resonance enhancement (Figure 7, middle) is analogous to Feynman pathways that contribute to two-photon absorption or "Raman-active modes" mentioned in vibrational sum-frequency generation studies.[85] As the transition probed under this resonance condition sits at the sum of the frequencies of the WL and upconversion fields, scanning the frequency of the upconversion field will induce summing with different frequency components of the spectrally broad WL field to give an ESFG signal at the same output frequency. Lastly, there is a doubly resonant condition (Figure 7, right) where two separate electronic states of a sample work in concert to give rise to the ESFG signal. As the upconversion pulse is scanned, a double resonance would give a change in the frequency of the ESFG signal intermediate to that expected for the one- and two-photon resonance conditions.

Figure 8A shows ESFG spectra of a 52 nm thick C1-PDI film as a function of the wavelength of the upconversion pulse. If

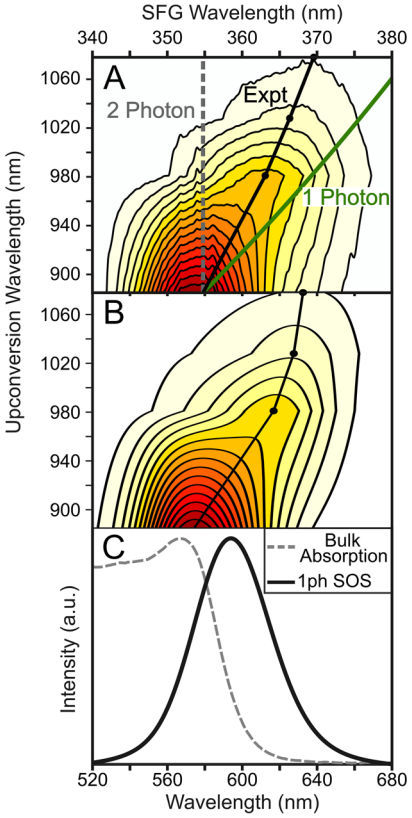

Figure 8. (A) PPP ESFG spectra of a 52 nm thick C1-PDI film as a function of the wavelength of the upconversion pulse. (B) ESFG spectra calculated using a sum-over-states (SOS) model. Black dots signify the maxima of spectra simulated for different upconversion wavelengths. (C) Comparison of the square modulus of the one-photon resonance found using the SOS model (black line) to the C1-PDI absorption spectrum (dashed gray line).

the ESFG signal is dominated by a two-photon resonance condition, we would expect to see intensity variations of the ESFG signal but no shift in the spectral position of its peaks as the wavelength of the upconversion pulse is varied (Figure 8A, gray dashed line). In contrast, if a one-photon resonance dominates the signal, the ESFG spectra should undergo a red-shift as the wavelength of the upconversion pulse increases (Figure 8A, green solid line). We see the peak of the ESFG spectra exhibits a shift with increasing upconversion wavelength that is intermediate between these two predictions, suggesting the spectra arise from a double-resonance condition.

We note this behavior is reminiscent of other systems where double-resonance contributions were found to dominate vibrational sum-frequency generation spectra.[44,98,99] These

https://dx.doi.org/10.1021/acs.jpcc.0c01025
J. Phys. Chem. C XXXX, XXX, XXX−XXX

spectra were able to be reproduced by using a sum-over-states (SOS) approach. As such, we have attempted to fit our ESFG response to a SOS model (Figure 8B) that multiplies a one-photon resonance line shape driven by the WL field with a pair of higher energy states that are accessed by the sum-frequency field. This model is similar to one used by Tahara and co-workers to describe ESFG spectra of oxazine 750 in water,[44] and its formulation is described in the Supporting Information. We find the SOS model gives excellent agreement with ESFG spectra in Figure 8A, recreating the red-shift of the most intense peak as the upconversion pulse is shifted to lower energy. This allows us to extract the one-photon resonance contribution to C1-PDI ESFG spectra. A corresponding fit to data for a C8-PDI film appears in the Supporting Information. Comparing the extracted one-photon resonance to the film's optical absorption spectrum shows the pronounced red-shift seen in ESFG spectra stems from a decrease in the C1-PDI bandgap of ~80 meV at the buried SiO_2 interface (Figure 8C).

Electronic Structure of the PDI:SiO_2 Interface. By accounting for thin film interference effects and double-resonance contributions to our ESFG spectra, we can extract the contribution to this data from both the PDI:Air and PDI:SiO_2 interfaces. The square modulus of the most important element to our ESFG spectra (χ_{yzy} for C1-PDI and χ_{yyz} for C8-PDI) is shown in Figure 9. Upon comparison

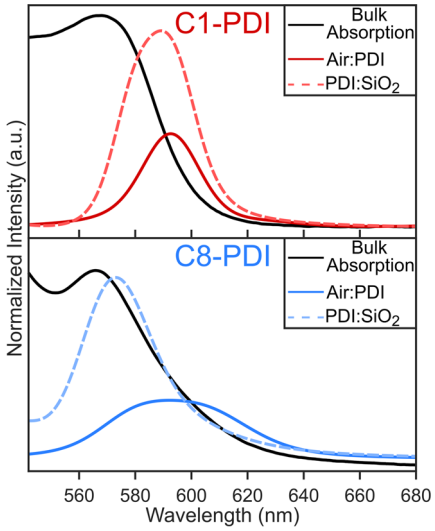

Figure 9. Comparison of the air exposed (Air:PDI) and buried (PDI:SiO_2) nonlinear susceptibilities: (top) C1-PDI $|\chi_{yzy}|^2$ and (bottom) C8-PDI $|\chi_{yyz}|^2$. Notice that both C1-PDI and C8-PDI possess buried interfacial nonlinear susceptibilities that are stronger than their air-exposed counterparts.

of the air:PDI and PDI:SiO_2 interfaces, it is apparent that the PDI:SiO_2 interface provides a larger response than its counterpart. This is not surprising; given the strong absorption properties of PDI derivatives in general, the WL field at the PDI:SiO_2 interface will be weaker than at the air:PDI interface, which necessitates that the PDI:SiO_2 susceptibility be sufficiently strong to yield near cancellation of the air:PDI signal as the film thickness is increased (Figure 5). As our films are textured, we attribute the origin of this difference in susceptibility strength to averaging induced by heterogeneity at the air:PDI interface. That is, because the air interface of our films possesses multiple crystallites that do not appear directionally oriented, this interface is likely more isotropic over the spatial region we probe, resulting in partial cancellation of the generated response.

The apparent red-shift of the PDI response at the SiO_2 interface relative to each material's bulk may arise from multiple sources. For instance, the SiO_2 surface may induce a solvatochromic narrowing of the interfacial PDI bandgap.[30] However, given SiO_2 has a similar dielectric constant as the PDI derivatives, and both C1-PDI and C8-PDI exhibit as much, if not more, of a spectral shift at the air:PDI interface, this effect would seem minor. Another potential explanation for the bandgap narrowing is formation of hybrid surface states that span the PDI:SiO_2 interface that result from charge donation from PDI to SiO_2, as has recently been observed in conjugated polymer:gold interfaces.[100] However, as SiO_2 is a wide bandgap insulator, any hybridization between SiO_2 and PDI valence states is highly unlikely.

Instead, we believe the changes result from subtle, strain-induced alteration of the PDI crystallite structure at the SiO_2 interface. As noted here and elsewhere[31,35,59,69,101] small changes to the slip-stack arrangement of neighboring molecules greatly modulates the solid-state electronic and photophysical properties of PDI molecular solids. In addition, given the lattice mismatch between the SiO_2 substrate and organic film, there can be pronounced changes in PDI packing when moving from the interface to the bulk.[72,73,102−104] Thus, small (subangstrom) changes in molecular packing seem a reasonable candidate for the apparent narrowing of each film's interfacial bandgap.

To test this hypothesis, we employed the tight-binding Hamiltonian used to fit absorption spectra of C1-PDI and C8-PDI films to estimate how the electronic density of states of stacks of each PDI change as they are slipped along their short and long-axes (Figure 10A,C). As our experimental data possess doubly resonant character, this complicates the calculation of ESFG line shapes using this model as it assumes only a single resonance contributes to spectra. As such, we forego comparing line shapes calculated using this model against ESFG data and focus solely on computing how the lowest-energy eigenstate of each PDI changes as a function of slip displacement between neighboring molecules. We scan over reasonable values for how this displacement may change due to strain at the SiO_2 interface to identify configurations where a transition between the PDI ground state and its first excited eigenstate match the spectral position of the PDI band edge inferred from our ESFG spectra (Figure 10B,D).

For C1-PDI, this model predicts the lowest energy eigenstate can experience the ~80 meV shift we observed in our ESFG data as a result of only a 0.75 Å displacement from the slip-stacking structure it adopts in molecular crystals (Figure 10A). For the C8-PDI ESFG response, we find the band edge shift inferred from ESFG spectra (~10 meV) can be accounted for by an even smaller shift of ~0.1 Å from its native slip-stacking geometry (Figure 10C). This trend is encouraging; as C8-PDI molecules possess a much longer alkyl chain compared to C1-PDI, C8-PDI molecules have additional degrees of freedom that allow them to adapt to external strain without needing to perturb the intermolecular ordering of their perylene cores. As C8-PDI was found to pack in similar ways on Al_2O_3 and SiO_2, it is reasonable to believe the interface plays a less important role in packing.[72,73] This suggests efforts to structurally engineer the packing of PDI and related molecules in bulk solids to achieve processes such as SF and

https://dx.doi.org/10.1021/acs.jpcc.0c01025
J. Phys. Chem. C XXXX, XXX, XXX−XXX

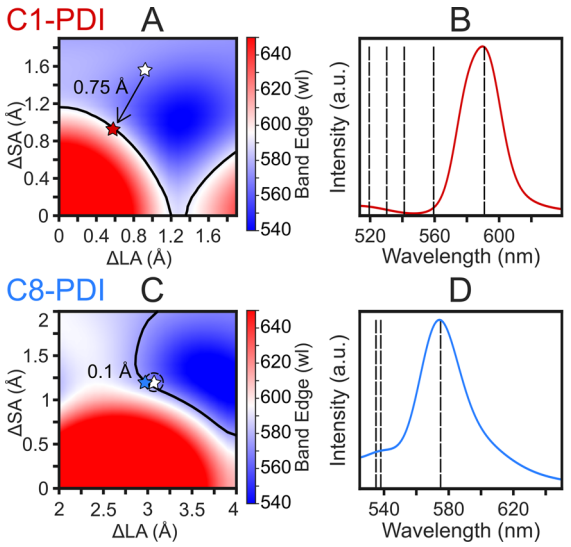

Figure 10. PDI lowest exciton energy shifts due to changes in slip displacement for C1-PDI and C8-PDI computed by using our tight-binding Hamiltonian. (A) Pseudocolor map depicting the lowest exciton energy of C1-PDI as a function of the short axis (ΔSA) and long axis (ΔLA) displacement between neighboring PDI molecules. The white star highlights the bulk C1-PDI structure while solid lines denote structures with an exciton energy that matches that of the PDI:SiO_2 interface inferred from ESFG spectra. The smallest structural perturbation needed from the bulk crystal structure to achieve this exciton energy is highlighted by the red star, which corresponds to a change in slip displacement of 0.75 Å. (B) Comparison of first and higher exciton energies for the displacement highlighted by the red star (dashed lines) against the $|\chi_{yzy}|^2$ element of the C1-PDI ESFG response at the PDI:SiO_2 interface (solid). (C, D) Equivalent plots as (A, B) but for C8-PDI. The blue star in panel A denotes the smallest structural perturbation from the C8-PDI bulk crystal structure at the PDI:SiO_2 interface consistent with our ESFG spectra. This corresponds to a change in slip displacement of 0.1 Å. Panel D plots the $|\chi_{yyz}|^2$ element of the C8-PDI:SiO_2 interface rather than $|\chi_{yzy}|^2$.

triplet energy transfer can be preserved at an interface if the molecules possess a sufficient buffer layer that can adsorb strain.

SUMMARY AND CONCLUSIONS

By looking at a combination of bulk and interface-specific data for C1-PDI and C8-PDI films, we have shown each material undergoes a change in its electronic density of states at material interfaces. These changes vary between derivatives and correlate with differences in the long-range ordering of each film. We attribute the changes in the interfacial density of states for these molecules to slight modifications of their slip-stack arrangement at the SiO_2 interface compared to their bulk. Our results highlight that ESFG directly complements existing thin-film structural probes, providing a nondestructive measure of buried interfacial structure.

More broadly, our experiments suggest C1-PDI and C8-PDI films each undergo a small structural change that enhances spatial overlap of their PDI cores at the SiO_2 interface. This overlap increases intermolecular electronic coupling, which reduces the PDI bandgap at the interface and potentially creates an energetic gradient that might funnel excitons toward the interface. Given the propensity of PDI derivatives to undergo efficient singlet fission, such a gradient could prove useful for moving energy to semiconductor charge collectors, such as silicon. In addition, the stronger coupling strengths that give rise to a narrowing of the PDI bandgap may enhance triplet transport to the interface as these excitons must travel via orbital overlap. Additional studies investigating how control of PDI interfacial structure impacts spin-triplet exciton extraction are warranted.

ASSOCIATED CONTENT

Supporting Information

The Supporting Information is available free of charge at https://pubs.acs.org/doi/10.1021/acs.jpcc.0c01025.

Description of the thin-film interference model, sum-over-states model, and tight-binding Hamiltonian used to describe ESFG spectra, along with additional fits to ESFG spectra produced by these models; comparison of the spectral bandwidth addressable by our ESFG spectrometer and absorption spectra of C1-PDI and C8-PDI films (PDF)

AUTHOR INFORMATION

Corresponding Author

Sean T. Roberts − *Department of Chemistry, The University of Texas at Austin, Austin, Texas 78712-1224, United States;* orcid.org/0000-0002-3322-3687; Email: roberts@cm.utexas.edu

Authors

Daniel E. Cotton − *Department of Chemistry, The University of Texas at Austin, Austin, Texas 78712-1224, United States;* orcid.org/0000-0002-5170-7108

Aaron P. Moon − *Department of Chemistry, The University of Texas at Austin, Austin, Texas 78712-1224, United States*

Complete contact information is available at: https://pubs.acs.org/10.1021/acs.jpcc.0c01025

Notes

The authors declare no competing financial interest.

ACKNOWLEDGMENTS

This work was supported by the National Science Foundation (CAREER Award: CHE-1654404), the Robert A. Welch Foundation (Grant F-1885), and the W. M. Keck Foundation (Grant 22605). The authors also gratefully acknowledge Jon A. Bender for aid in preparation of PDI thin films and their characterization via spectroscopic ellipsometry. The authors also acknowledge the Texas Advanced Computing Center (TACC) for computational resources provided for spectroscopic calculations and the Texas Materials Institute (TMI) at UT Austin for use of equipment for film deposition, GIWAXS, and ellipsometry measurements.

REFERENCES

(1) Lewis, N. S. Research Opportunities to Advance Solar Energy Utilization. *Science* **2016**, *351*, aad1920.

(2) Rao, A.; Friend, R. H. Harnessing Singlet Exciton Fission to Break the Shockley−Queisser Limit. *Nat. Rev. Mater.* **2017**, *2*, 17063.

(3) Pazos-Outón, L. M.; Lee, J. M.; Futscher, M. H.; Kirch, A.; Tabachnyk, M.; Friend, R. H.; Ehrler, B. A Silicon−Singlet Fission Tandem Solar Cell Exceeding 100% External Quantum Efficiency with High Spectral Stability. *ACS Energy Lett.* **2017**, *2*, 476−480.

(4) Louwen, A.; van Sark, W.; Schropp, R.; Faaij, A. A Cost Roadmap for Silicon Heterojunction Solar Cells. *Sol. Energy Mater. Sol. Cells* **2016**, *147*, 295−314.
(5) Richter, A.; Hermle, M.; Glunz, S. W. Reassessment of the Limiting Efficiency for Crystalline Silicon Solar Cells. *IEEE J. Photovolt.* **2013**, *3*, 1184−1191.
(6) Futscher, M. H.; Rao, A.; Ehrler, B. The Potential of Singlet Fission Photon Multipliers as an Alternative to Silicon-Based Tandem Solar Cells. *ACS Energy Lett.* **2018**, *3*, 2587−2592.
(7) Gish, M. K.; Pace, N. A.; Rumbles, G.; Johnson, J. C. Emerging Design Principles for Enhanced Solar Energy Utilization with Singlet Fission. *J. Phys. Chem. C* **2019**, *123*, 3923−3934.
(8) Hanna, M. C.; Nozik, A. J. Solar Conversion Efficiency of Photovoltaic and Photoelectrolysis Cells with Carrier Multiplication Absorbers. *J. Appl. Phys.* **2006**, *100*, 074510.
(9) Tayebjee, M. J. Y.; McCamey, D. R.; Schmidt, T. W. Beyond Shockley−Queisser: Molecular Approaches to High-Efficiency Photovoltaics. *J. Phys. Chem. Lett.* **2015**, *6*, 2367−2378.
(10) Merrifield, R. E. Magnetic Effects on Triplet Exciton Interactions. *Pure Appl. Chem.* **1971**, *27*, 481−498.
(11) Smith, M. B.; Michl, J. Singlet Fission. *Chem. Rev.* **2010**, *110*, 6891−6936.
(12) Smith, M. B.; Michl, J. Recent Advances in Singlet Fission. *Annu. Rev. Phys. Chem.* **2013**, *64*, 361−386.
(13) Miyata, K.; Conrad-Burton, F. S.; Geyer, F. L.; Zhu, X.-Y. Triplet Pair States in Singlet Fission. *Chem. Rev.* **2019**, *119*, 4261−4292.
(14) Scholes, G. D. Correlated Pair States Formed by Singlet Fission and Exciton−Exciton Annihilation. *J. Phys. Chem. A* **2015**, *119*, 12699−12705.
(15) Musser, A. J.; Clark, J. Triplet-Pair States in Organic Semiconductors. *Annu. Rev. Phys. Chem.* **2019**, *70*, 323−351.
(16) Wilson, M. W. B.; Rao, A.; Clark, J.; Kumar, R. S. S.; Brida, D.; Cerullo, G.; Friend, R. H. Ultrafast Dynamics of Exciton Fission in Polycrystalline Pentacene. *J. Am. Chem. Soc.* **2011**, *133*, 11830−11833.
(17) Yost, S. R.; Lee, J.; Wilson, M. W. B.; Wu, T.; McMahon, D. P.; Parkhurst, R. R.; Thompson, N. J.; Congreve, D. N.; Rao, A.; Johnson, K.; et al. A Transferable Model for Singlet-Fission Kinetics. *Nat. Chem.* **2014**, *6*, 492−497.
(18) Dexter, D. L. Two Ideas on Energy Transfer Phenomena: Ion-Pair Effects Involving the OH Stretching Mode, and Sensitization of Photovoltaic Cells. *J. Lumin.* **1979**, *18−19*, 779−784.
(19) Einzinger, M.; Wu, T.; Kompalla, J. F.; Smith, H. L.; Perkinson, C. F.; Nienhaus, L.; Wieghold, S.; Congreve, D. N.; Kahn, A.; Bawendi, M. G.; Baldo, M. A. Sensitization of Silicon by Singlet Exciton Fission in Tetracene. *Nature* **2019**, *571*, 90−94.
(20) Xia, P.; Raulerson, E. K.; Coleman, D.; Gerke, C. S.; Mangolini, L.; Tang, M. L.; Roberts, S. T. Achieving Spin-Triplet Exciton Transfer between Silicon and Molecular Acceptors for Photon Upconversion. *Nat. Chem.* **2020**, *12*, 137−144.
(21) Burdett, J. J.; Gosztola, D.; Bardeen, C. J. The Dependence of Singlet Exciton Relaxation on Excitation Density and Temperature in Polycrystalline Tetracene Thin Films: Kinetic Evidence for a Dark Intermediate State and Implications for Singlet Fission. *J. Chem. Phys.* **2011**, *135*, 214508.
(22) Roberts, S. T.; McAnally, R. E.; Mastron, J. N.; Webber, D. H.; Whited, M. T.; Brutchey, R. L.; Thompson, M. E.; Bradforth, S. E. Efficient Singlet Fission Discovered in a Disordered Acene Film. *J. Am. Chem. Soc.* **2012**, *134*, 6388−6400.
(23) Eaton, S. W.; Shoer, L. E.; Karlen, S. D.; Dyar, S. M.; Margulies, E. A.; Veldkamp, B. S.; Ramanan, C.; Hartzler, D. A.; Savikhin, S.; Marks, T. J.; Wasielewski, M. R. Singlet Exciton Fission in Polycrystalline Thin Films of a Slip-Stacked Perylenediimide. *J. Am. Chem. Soc.* **2013**, *135*, 14701−14712.
(24) Le, A. K.; Bender, J. A.; Arias, D. H.; Cotton, D. E.; Johnson, J. C.; Roberts, S. T. Singlet Fission Involves an Interplay between Energetic Driving Force and Electronic Coupling in Perylenediimide Films. *J. Am. Chem. Soc.* **2018**, *140*, 814−826.
(25) Wang, C.; Tauber, M. J. High-Yield Singlet Fission in a Zeaxanthin Aggregate Observed by Picosecond Resonance Raman Spectroscopy. *J. Am. Chem. Soc.* **2010**, *132*, 13988−13991.
(26) Lukman, S.; Richter, J. M.; Yang, L.; Hu, P.; Wu, J.; Greenham, N. C.; Musser, A. J. Efficient Singlet Fission and Triplet-Pair Emission in a Family of Zethrene Diradicaloids. *J. Am. Chem. Soc.* **2017**, *139*, 18376−18385.
(27) Mauck, C. M.; Hartnett, P. E.; Wu, Y.-L.; Miller, C. E.; Marks, T. J.; Wasielewski, M. R. Singlet Fission within Diketopyrrolopyrrole Nanoparticles in Water. *Chem. Mater.* **2017**, *29*, 6810−6817.
(28) Piland, G. B.; Burdett, J. J.; Hung, T.-Y.; Chen, P.-H.; Lin, C.-F.; Chiu, T.-L.; Lee, J.-H.; Bardeen, C. J. Dynamics of Molecular Excitons near a Semiconductor Surface Studied by Fluorescence Quenching of Polycrystalline Tetracene on Silicon. *Chem. Phys. Lett.* **2014**, *601*, 33−38.
(29) MacQueen, R. W.; Liebhaber, M.; Niederhausen, J.; Mews, M.; Gersmann, C.; Jäckle, S.; Jäger, K.; Tayebjee, M. J. Y.; Schmidt, T. W.; Rech, B.; Lips, K. Crystalline Silicon Solar Cells with Tetracene Interlayers: The Path to Silicon-Singlet Fission Heterojunction Devices. *Mater. Horiz.* **2018**, *5*, 1065−1075.
(30) Yost, S. R.; Van Voorhis, T. Electrostatic Effects at Organic Semiconductor Interfaces: A Mechanism for "Cold" Exciton Breakup. *J. Phys. Chem. C* **2013**, *117*, 5617−5625.
(31) Farag, M. H.; Krylov, A. I. Singlet Fission in Perylenediimide Dimers. *J. Phys. Chem. C* **2018**, *122*, 25753−25763.
(32) Chen, Y.; Tamblyn, I.; Quek, S. Y. Energy Level Alignment at Hybridized Organic−Metal Interfaces: The Role of Many-Electron Effects. *J. Phys. Chem. C* **2017**, *121*, 13125−13134.
(33) Rangan, S.; Ruggieri, C.; Bartynski, R.; Martínez, J. I.; Flores, F.; Ortega, J. Adsorption Geometry and Energy Level Alignment at the PTCDA/TiO_2 (110) Interface. *J. Phys. Chem. B* **2018**, *122*, 534−542.
(34) Martinez, J. I.; Flores, F.; Ortega, J.; Rangan, S.; Ruggieri, C. M.; Bartynski, R. A. Unveiling Universal Trends for the Energy Level Alignment in Organic/Oxide Interfaces. *Phys. Chem. Chem. Phys.* **2017**, *19*, 24412−24420.
(35) Hestand, N. J.; Tempelaar, R.; Knoester, J.; Jansen, T. L. C.; Spano, F. C. Exciton Mobility Control through sub-Å Packing Modifications in Molecular Crystals. *Phys. Rev. B: Condens. Matter Mater. Phys.* **2015**, *91*, 195315.
(36) Hestand, N. J.; Spano, F. C. Molecular Aggregate Photophysics beyond the Kasha Model: Novel Design Principles for Organic Materials. *Acc. Chem. Res.* **2017**, *50*, 341−350.
(37) Coropceanu, V.; Cornil, J.; da Silva Filho, D. A.; Olivier, Y.; Silbey, R.; Brédas, J.-L. Charge Transport in Organic Semiconductors. *Chem. Rev.* **2007**, *107*, 926−952.
(38) Ryno, S. M.; Fu, Y.-T.; Risko, C.; Brédas, J.-L. Polarization Energies at Organic−Organic Interfaces: Impact on the Charge Separation Barrier at Donor−Acceptor Interfaces in Organic Solar Cells. *ACS Appl. Mater. Interfaces* **2016**, *8*, 15524−15534.
(39) Ryno, S. M.; Risko, C.; Brédas, J.-L. Impact of Molecular Orientation and Packing Density on Electronic Polarization in the Bulk and at Surfaces of Organic Semiconductors. *ACS Appl. Mater. Interfaces* **2016**, *8*, 14053−14062.
(40) Austin, A.; Hestand, N. J.; McKendry, I. G.; Zhong, C.; Zhu, X.; Zdilla, M. J.; Spano, F. C.; Szarko, J. M. Enhanced Davydov Splitting in Crystals of a Perylene Diimide Derivative. *J. Phys. Chem. Lett.* **2017**, *8*, 1118−1123.
(41) Vasseur, K.; Rolin, C.; Vandezande, S.; Temst, K.; Froyen, L.; Heremans, P. A Growth and Morphology Study of Organic Vapor Phase Deposited Perylene Diimide Thin Films for Transistor Applications. *J. Phys. Chem. C* **2010**, *114*, 2730−2737.
(42) Takahashi, Y.; Mikasa, T.; Hayakawa, K.; Yokokura, S.; Hasegawa, H.; Harada, J.; Inabe, T. Fabrication of Conducting Thin Films on the Surfaces of 7,7,8,8-Tetracyanoquinodimethane Single-Component and Charge-Transfer Complex Single Crystals: Nucleation, Crystal Growth, Morphology, and Charge Transport. *J. Phys. Chem. C* **2016**, *120*, 17537−17545.

https://dx.doi.org/10.1021/acs.jpcc.0c01025
J. Phys. Chem. C XXXX, XXX, XXX−XXX

(43) Griffin, M. P.; Gearba, R.; Stevenson, K. J.; Vanden Bout, D. A.; Dolocan, A. Revealing the Chemistry and Morphology of Buried Donor/Acceptor Interfaces in Organic Photovoltaics. *J. Phys. Chem. Lett.* **2017**, *8*, 2764−2773.
(44) Yamaguchi, S.; Tahara, T. Determining Electronic Spectra at Interfaces by Electronic Sum Frequency Generation: One- and Two-Photon Double Resonant Oxazine 750 at the Air/Water Interface. *J. Chem. Phys.* **2006**, *125*, 194711.
(45) Yamaguchi, S.; Tahara, T. Development of Electronic Sum Frequency Generation Spectroscopies and Their Application to Liquid Interfaces. *J. Phys. Chem. C* **2015**, *119*, 14815−14828.
(46) Rizzuto, A. M.; Irgen-Gioro, S.; Eftekhari-Bafrooei, A.; Saykally, R. J. Broadband Deep UV Spectra of Interfacial Aqueous Iodide. *J. Phys. Chem. Lett.* **2016**, *7*, 3882−3885.
(47) Lin, C.-K.; Lei, J.; Lin, Y.-D.; Lin, S. H. Electronic Sum-Frequency Generation (ESFG) Spectroscopy: Theoretical Formulation of Resonances with Symmetry-Allowed and Symmetry-Forbidden Electronic Excited States. *Mol. Phys.* **2017**, *115*, 1803−1812.
(48) Watson, B. R.; Doughty, B.; Calhoun, T. R. Energetics at the Surface: Direct Optical Mapping of Core and Surface Electronic Structure in CdSe Quantum Dots Using Broadband Electronic Sum Frequency Generation Microspectroscopy. *Nano Lett.* **2019**, *19*, 6157−6165.
(49) Kelley, A. M. Can Second Order Nonlinear Spectroscopies Selectively Probe Optically "Dark" Surface States in Small Semiconductor Nanocrystals? *J. Chem. Phys.* **2020**, *152*, 120901.
(50) Foglia, L.; Wolf, M.; Stähler, J. Ultrafast Dynamics in Solids Probed by Femtosecond Time-Resolved Broadband Electronic Sum Frequency Generation. *Appl. Phys. Lett.* **2016**, *109* (20), 202106.
(51) Moon, A. P.; Pandey, R.; Bender, J. A.; Cotton, D. E.; Renard, B. A.; Roberts, S. T. Using Heterodyne-Detected Electronic Sum Frequency Generation to Probe the Electronic Structure of Buried Interfaces. *J. Phys. Chem. C* **2017**, *121*, 18653−18664.
(52) Pandey, R.; Moon, A. P.; Bender, J. A.; Roberts, S. T. Extracting the Density of States of Copper Phthalocyanine at the SiO_2 Interface with Electronic Sum Frequency Generation. *J. Phys. Chem. Lett.* **2016**, *7*, 1060−1066.
(53) Li, Y.; Wang, J.; Xiong, W. Probing Electronic Structures of Organic Semiconductors at Buried Interfaces by Electronic Sum Frequency Generation Spectroscopy. *J. Phys. Chem. C* **2015**, *119*, 28083−28089.
(54) Deng, G.-H.; Qian, Y.; Rao, Y. Development of Ultrafast Broadband Electronic Sum Frequency Generation for Charge Dynamics at Surfaces and Interfaces. *J. Chem. Phys.* **2019**, *150*, No. 024708.
(55) Deng, G.-H.; Qian, Y.; Wei, Q.; Zhang, T.; Rao, Y. Interface-Specific Two-Dimensional Electronic Sum Frequency Generation Spectroscopy. *J. Phys. Chem. Lett.* **2020**, *11*, 1738−1745.
(56) Shen, Y. R. *The Principles of Nonlinear Optics*; Wiley-Interscience: New York, 1984.
(57) Yamaguchi, S.; Tahara, T. Heterodyne-Detected Electronic Sum Frequency Generation: "Up" versus "down" Alignment of Interfacial Molecules. *J. Chem. Phys.* **2008**, *129*, 101102.
(58) Kusaka, R.; Ishiyama, T.; Nihonyanagi, S.; Morita, A.; Tahara, T. Structure at the Air/Water Interface in the Presence of Phenol: A Study Using Heterodyne-Detected Vibrational Sum Frequency Generation and Molecular Dynamics Simulation. *Phys. Chem. Chem. Phys.* **2018**, *20*, 3002−3009.
(59) Le, A. K.; Bender, J. A.; Roberts, S. T. Slow Singlet Fission Observed in a Polycrystalline Perylenediimide Thin Film. *J. Phys. Chem. Lett.* **2016**, *7*, 4922−4928.
(60) Wurthner, F. Perylene Bisimide Dyes as Versatile Building Blocks for Functional Supramolecular Architectures. *Chem. Commun.* **2004**, *14*, 1564−1579.
(61) Ford, W. E.; Kamat, P. V. Photochemistry of 3,4,9,10-Perylenetetracarboxylic Dianhydride Dyes. 3. Singlet and Triplet Excited-State Properties of the Bis(2,5-Di-Tert-Butylphenyl)Imide Derivative. *J. Phys. Chem.* **1987**, *91*, 6373−6380.
(62) Löhmannsröben, H. G.; Langhals, H. Laser Performance of Perylenebis(dicarboximide) Dyes with Long Secondary Alkyl Chains. *Appl. Phys. B: Photophys. Laser Chem.* **1989**, *48*, 449−452.
(63) Nakazono, S.; Easwaramoorthi, S.; Kim, D.; Shinokubo, H.; Osuka, A. Synthesis of Arylated Perylene Bisimides through C−H Bond Cleavage under Ruthenium Catalysis. *Org. Lett.* **2009**, *11*, 5426−5429.
(64) Langhals, H.; Karolin, J.; Johansson, L. B.-A. Spectroscopic Properties of New and Convenient Standards for Measuring Fluorescence Quantum Yields. *J. Chem. Soc., Faraday Trans.* **1998**, *94*, 2919−2922.
(65) Huang, C.; Barlow, S.; Marder, S. R. Perylene-3,4,9,10-Tetracarboxylic Acid Diimides: Synthesis, Physical Properties, and Use in Organic Electronics. *J. Org. Chem.* **2011**, *76*, 2386−2407.
(66) Kazmaier, P. M.; Hoffmann, R. A Theoretical Study of Crystallochromy. Quantum Interference Effects in the Spectra of Perylene Pigments. *J. Am. Chem. Soc.* **1994**, *116*, 9684−9691.
(67) O'Brien, D. B.; Massari, A. M. Modeling Multilayer Thin Film Interference Effects in Interface-Specific Coherent Nonlinear Optical Spectroscopies. *J. Opt. Soc. Am. B* **2013**, *30*, 1503−1503.
(68) Briseno, A. L.; Mannsfeld, S. C. B.; Reese, C.; Hancock, J. M.; Xiong, Y.; Jenekhe, S. A.; Bao, Z.; Xia, Y. Perylenediimide Nanowires and Their Use in Fabricating Field-Effect Transistors and Complementary Inverters. *Nano Lett.* **2007**, *7*, 2847−2853.
(69) Klebe, G.; Graser, F.; Hädicke, E.; Berndt, J. Crystallochromy as a Solid-State Effect: Correlation of Molecular Conformation, Crystal Packing and Colour in Perylene-3,4:9,10-Bis(Dicarboximide) Pigments. *Acta Crystallogr., Sect. B: Struct. Sci.* **1989**, *45*, 69−77.
(70) Hädicke, E.; Graser, F. Structures of Eleven Perylene-3,4:9,10-Bis(Dicarboximide) Pigments. *Acta Crystallogr., Sect. C: Cryst. Struct. Commun.* **1986**, *42* (2), 189−195.
(71) Yanagi, H.; Toda, Y.; Noguchi, T. Photoelectrochemical Behaviors of Orientation-Controlled Thin Films of *N,N′*-Substituted Perylene-3,4:9,10-Bis(dicarboximide). *Jpn. J. Appl. Phys.* **1995**, *34*, 3808−3813.
(72) Krauss, T. N.; Barrena, E.; Zhang, X. N.; de Oteyza, D. G.; Major, J.; Dehm, V.; Würthner, F.; Cavalcanti, L. P.; Dosch, H. Three-Dimensional Molecular Packing of Thin Organic Films of PTCDI-C_8 Determined by Surface X-Ray Diffraction. *Langmuir* **2008**, *24*, 12742−12744.
(73) Krauss, T. N.; Barrena, E.; de Oteyza, D. G.; Zhang, X. N.; Major, J.; Dehm, V.; Würthner, F.; Dosch, H. X-Ray/Atomic Force Microscopy Study of the Temperature-Dependent Multilayer Structure of PTCDI-C_8 Films on SiO_2. *J. Phys. Chem. C* **2009**, *113*, 4502−4506.
(74) Ferguson, A. J.; Jones, T. S. Photophysics of PTCDA and Me-PTCDI Thin Films: Effects of Growth Temperature. *J. Phys. Chem. B* **2006**, *110*, 6891−6898.
(75) Ferguson, A. J.; Jones, T. S. Spectroscopic Evidence for Aggregate Formation in N,N′-Bis(Phenylethyl)-Perylene-3,4,9,10-Bis(Dicarboximide) (PPEI) Films Grown at Room-Temperature. *Chem. Phys. Lett.* **2009**, *474*, 137−140.
(76) Gisslén, L.; Scholz, R. Crystallochromy of Perylene Pigments: Interference between Frenkel Excitons and Charge-Transfer States. *Phys. Rev. B: Condens. Matter Mater. Phys.* **2009**, *80*, 115309.
(77) Hoffmann, M.; Schmidt, K.; Fritz, T.; Hasche, T.; Agranovich, V. M.; Leo, K. The Lowest Energy Frenkel and Charge-Transfer Excitons in Quasi-One-Dimensional Structures: Application to MePTCDI and PTCDA Crystals. *Chem. Phys.* **2000**, *258*, 73−96.
(78) Oleson, A.; Zhu, T.; Dunn, I. S.; Bialas, D.; Bai, Y.; Zhang, W.; Dai, M.; Reichman, D. R.; Tempelaar, R.; Huang, L.; et al. Perylene Diimide-Based Hj- and hJ-Aggregates: The Prospect of Exciton Band Shape Engineering in Organic Materials. *J. Phys. Chem. C* **2019**, *123*, 20567−20578.
(79) O'Brien, D. B.; Massari, A. M. Experimental Evidence for an Optical Interference Model for Vibrational Sum Frequency Generation on Multilayer Organic Thin Film Systems I: Electric Dipole Approximation. *J. Chem. Phys.* **2015**, *142*, No. 024703.

https://dx.doi.org/10.1021/acs.jpcc.0c01025
J. Phys. Chem. C XXXX, XXX, XXX−XXX

(80) O'Brien, D. B.; Massari, A. M. Experimental Evidence for an Optical Interference Model for Vibrational Sum Frequency Generation on Multilayer Organic Thin Film Systems. II. Consideration for Higher Order Terms. *J. Chem. Phys.* **2015**, *142*, No. 024704.
(81) Azam, Md. S.; Cai, C.; Hore, D. K. Selective Probing of Thin Film Interfaces Using Internal Reflection Sum-Frequency Spectroscopy. *J. Phys. Chem. C* **2019**, *123*, 23535−23544.
(82) FitzGerald, W. R.; Jena, K. C.; Hore, D. K. Effects of Single-Source Multiple Beam Interference in Vibrational Sum Frequency Generation Spectroscopy. *J. Mol. Struct.* **2015**, *1084*, 368−373.
(83) McGall, S. J.; Davies, P. B.; Neivandt, D. J. Interference Effects in Sum Frequency Vibrational Spectra of Thin Polymer Films: An Experimental and Modeling Investigation. *J. Phys. Chem. B* **2004**, *108*, 16030−16039.
(84) Guyot-Sionnest, P.; Shen, Y. R. Bulk Contribution in Surface Second-Harmonic Generation. *Phys. Rev. B: Condens. Matter Mater. Phys.* **1988**, *38*, 7985−7989.
(85) Matsuzaki, K.; Nihonyanagi, S.; Yamaguchi, S.; Nagata, T.; Tahara, T. Vibrational Sum Frequency Generation by the Quadrupolar Mechanism at the Nonpolar Benzene/Air Interface. *J. Phys. Chem. Lett.* **2013**, *4*, 1654−1658.
(86) Craig, I. M.; Tassone, C. J.; Tolbert, S. H.; Schwartz, B. J. Second-Harmonic Generation in Conjugated Polymer Films: A Sensitive Probe of How Bulk Polymer Crystallinity Changes with Spin Speed. *J. Chem. Phys.* **2010**, *133*, No. 044901.
(87) Held, H.; Lvovsky, A. I.; Wei, X.; Shen, Y. R. Bulk Contribution from Isotropic Media in Surface Sum-Frequency Generation. *Phys. Rev. B: Condens. Matter Mater. Phys.* **2002**, *66*, 205110.
(88) Shen, Y. R. Surface Contribution versus Bulk Contribution in Surface Nonlinear Optical Spectroscopy. *Appl. Phys. B: Lasers Opt.* **1999**, *68*, 295−300.
(89) Rahimi, R.; Narang, V.; Korakakis, D. Optical and Morphological Studies of Thermally Evaporated PTCDI-C_8 Thin Films for Organic Solar Cell Applications. *Int. J. Photoenergy* **2013**, *2013*, 1.
(90) Zykov, A.; Bommel, S.; Wolf, C.; Pithan, L.; Weber, C.; Beyer, P.; Santoro, G.; Rabe, J. P.; Kowarik, S. Diffusion and Nucleation in Multilayer Growth of PTCDI-C_8 Studied with *in Situ* X-Ray Growth Oscillations and Real-Time Small Angle X-Ray Scattering. *J. Chem. Phys.* **2017**, *146*, No. 052803.
(91) Tian, C. S.; Shen, Y. R. Recent Progress on Sum-Frequency Spectroscopy. *Surf. Sci. Rep.* **2014**, *69*, 105−131.
(92) Zhuang, X.; Miranda, P. B.; Kim, D.; Shen, Y. R. Mapping Molecular Orientation and Conformation at Interfaces by Surface Nonlinear Optics. *Phys. Rev. B: Condens. Matter Mater. Phys.* **1999**, *59*, 12632−12640.
(93) Pugh, D.; Morley, J. O. Molecular Hyperpolarizabilities of Organic Materials. In *Nonlinear Optical Properties of Organic Molecules and Crystals*; Elsevier: 1987; pp 193−225.
(94) Moad, A. J.; Simpson, G. J. A Unified Treatment of Selection Rules and Symmetry Relations for Sum-Frequency and Second Harmonic Spectroscopies. *J. Phys. Chem. B* **2004**, *108*, 3548−3562.
(95) Hirose, C.; Akamatsu, N.; Domen, K. Formulas for the Analysis of Surface Sum-frequency Generation Spectrum by CH Stretching Modes of Methyl and Methylene Groups. *J. Chem. Phys.* **1992**, *96*, 997−1004.
(96) Tafipolsky, M.; Engels, B. Accurate Intermolecular Potentials with Physically Grounded Electrostatics. *J. Chem. Theory Comput.* **2011**, *7*, 1791−1803.
(97) Tsiper, E. V.; Soos, Z. G. Charge Redistribution and Polarization Energy of Organic Molecular Crystals. *Phys. Rev. B: Condens. Matter Mater. Phys.* **2001**, *64*, 195124.
(98) Raschke, M. B.; Hayashi, M.; Lin, S. H.; Shen, Y. R. Doubly-Resonant Sum-Frequency Generation Spectroscopy for Surface Studies. *Chem. Phys. Lett.* **2002**, *359*, 367−372.
(99) Hayashi, M.; Lin, S. H.; Raschke, M. B.; Shen, Y. R. A Molecular Theory for Doubly Resonant IR−UV-Vis Sum-Frequency Generation. *J. Phys. Chem. A* **2002**, *106*, 2271−2282.
(100) Özçelik, V. O.; Li, Y.; Xiong, W.; Paesani, F. Modeling Spontaneous Charge Transfer at Metal/Organic Hybrid Heterostructures. *J. Phys. Chem. C* **2020**, *124*, 4802−4809.
(101) Mirjani, F.; Renaud, N.; Gorczak, N.; Grozema, F. C. Theoretical Investigation of Singlet Fission in Molecular Dimers: The Role of Charge Transfer States and Quantum Interference. *J. Phys. Chem. C* **2014**, *118*, 14192−14199.
(102) Belova, V.; Wagner, B.; Reisz, B.; Zeiser, C.; Duva, G.; Rozbořil, J.; Novák, J.; Gerlach, A.; Hinderhofer, A.; Schreiber, F. Real-Time Structural and Optical Study of Growth and Packing Behavior of Perylene Diimide Derivative Thin Films: Influence of Side-Chain Modification. *J. Phys. Chem. C* **2018**, *122*, 8589−8601.
(103) Jones, A. O. F.; Chattopadhyay, B.; Geerts, Y. H.; Resel, R. Substrate-Induced and Thin-Film Phases: Polymorphism of Organic Materials on Surfaces. *Adv. Funct. Mater.* **2016**, *26*, 2233−2255.
(104) Petit, M.; Hayakawa, R.; Wakayama, Y.; Chikyow, T. Early Stage of Growth of a Perylene Diimide Derivative Thin Film Growth on Various Si(001) Substrates. *J. Phys. Chem. C* **2007**, *111*, 12747−12751.

https://dx.doi.org/10.1021/acs.jpcc.0c01025
J. Phys. Chem. C XXXX, XXX, XXX−XXX